COMMUNICATION

# On-Chip Photonic Memory Elements Employing Phase-Change Materials

*Carlos Rios, Peiman Hosseini, C. David Wright, Harish Bhaskaran,\* and Wolfram H. P. Pernice\**

Phase-change materials (PCMs) based on chalcogenide compounds are capable of switching from the crystalline (amorphous) to the amorphous (crystalline) state on a picosecond timescale.[1–3] This property together with the ability of retaining the desired state for times spanning into decades[2,4] has allowed the development of non-volatile memories for removable optical data storage, such as the Blu-Ray disc, and, more recently, enabled phase-change random-access memories (PC-RAM).[5,6] The enormous property contrast in the electrical resistivity, as well as the optical reflectivity,[7–9] even at the nanoscale, can be precisely controlled either by means of optical pulses (in optical discs) or by electrical pulses (PC-RAM).[6,10–12] The widely tunable optical properties of PCMs are particularly attractive for on-chip photonics where predominantly passive materials are employed which lack efficient capabilities for static tunability. Complementary metal-oxide-semiconductor (CMOS) compatible materials, such as silicon, silicon nitride, and silicon dioxide, possess a centro-sysmmetric lattice structure,[13] prohibiting second-order non-linearity and the electro-optical effect frequently used for all-optical and electro-optical modulation.[14,15] PCMs on the other hand can be conveniently combined with existing silicon photonics technology enabling non-volatile data storage[16] with the additional benefit of information retention when the device is not powered in contrast to mechanical and other photonic memories.[17–19]

In this work, we implement hybrid nanophotonic-PCM circuits to realize tunable photonic devices based on nanoscale chalcogenide junctions. The alloy Ge$_2$Sb$_2$Te$_5$ (GST) is a near-ideal material for such a system, given that the material possesses one of the most pronounced contrasts in the dielectric function amongst known phase-change memory alloys.[2,20] Furthermore, the refractive index contrast is maintained over a broad spectral range covering visible and infrared wavelengths.[21] Using a memory element as illustrated in **Figure 1**a, the optical properties of such photonic integrated circuits can be dramatically altered by a nanoscale PCM section that is switched between its two crystallographic states. Upon switching, the light mode propagating inside the waveguide is modified through the interaction with GST as shown in Figure 1b,c. Because the complex propagation constant and thus the attenuation coefficient of the waveguide mode depends on the phase state of the GST, the transmission spectrum of the device is also strongly affected upon transition from the amorphous to the face-center cubic (fcc) crystalline phase. This is the basis for information storage in phase-sensitive photonic devices as demonstrated throughout this Communication. We further determine the attenuation coefficient of waveguide-PCM devices in dependence of wavelength, phase and geometry with three independent nanophotonic measurement concepts based on race-track resonators (Figure 1d), Mach–Zehnder interferometers (MZI) (Figure 1e) and balanced splitters (Figure 1f).

In order to enable broadband optical operation, the devices shown in Figure 1 were fabricated from silicon nitride-on-insulator substrates with 330 nm stoichiometric Si$_3$N$_4$ on 3300 nm buffered SiO$_2$, which allow us to obtain high-quality nanophotonic components with low propagation loss at telecom wavelengths.[22,23] Photonic circuitry is defined using a combination of electron-beam lithography and reactive ion etching as described in the experimental section. Here, we employ partially etched ridge waveguides in order to achieve optical confinement without requiring a large step height, which is important for the later deposition of the chalcogenide film. Using a lift-off procedure waveguide sections covered with 10 nm of GST are subsequently realized after a second lithography step and sputtering in argon atmosphere. In order to prevent oxidization of the GST, the PCM is capped with a thin layer of indium tin oxide (ITO). ITO is optically transparent for the entire visible spectrum and provides moderate loss at near-IR wavelengths,[24] which allows optical access to the active phase-change material layer with the added advantage of being highly conducting, paving the way for future work on electro-optical mixed mode devices.

To measure the optical transmission of the devices shown above, we used a customized measurement setup with an optical fiber array connected to a continuously tunable laser source (1.5–1.62 μm bandwidth) and low-noise photoreceivers. The on-chip counterpart consists of focusing Bragg gratings aligned to the fiber array, which couple light into the waveguides and collect the transmitted light from a second port, as shown in the bottom of Figure 1d–f.[22] In the case of the

C. Rios, Dr. W. H. P. Pernice
Institute for Nanotechnology (INT),
Karlsruhe Institute of Technology (KIT)
Hermann-von-Helmholtz-Platz 1, 76344, Germany
E-mail: wolfram.pernice@kit.edu
Dr. P. Hosseini, Dr. H. Bhaskaran
Department of Materials, University of Oxford
Parks Road, Oxford, OX1 3PH, United Kingdom
E-mail: harish.bhaskaran@materials.ox.ac.uk
Prof. C. D. Wright
College of Engineering, Mathematics and Physical Sciences
University of Exeter
Exeter, EX4 4QF, United Kingdom

Materials
Views
www.MaterialsViews.com

ADVANCED
MATERIALS
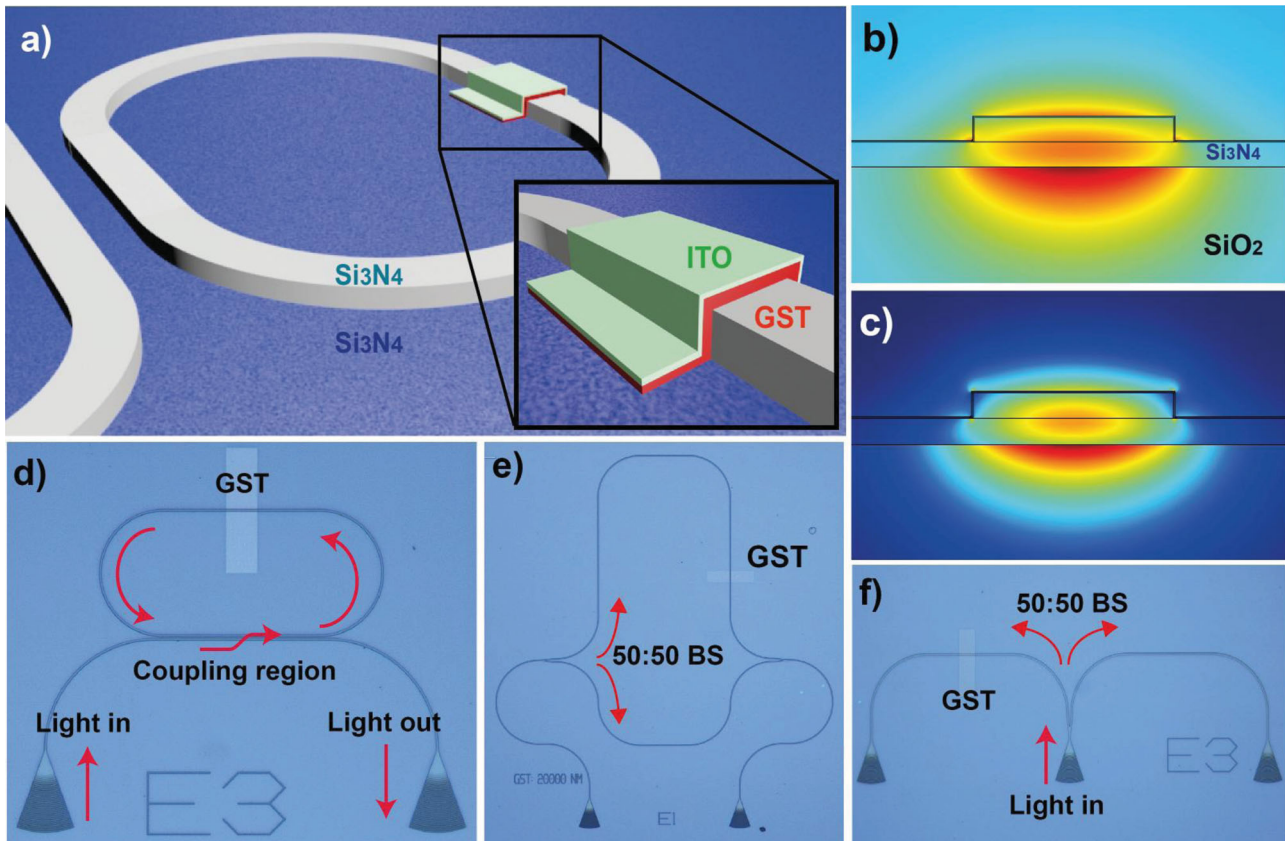www.advmat.de

COMMUNICATION

**Figure 1.** Hybrid nanophotonic-chalcogenide circuits. a) 3D scheme of the platform using partially etched ridge waveguides in Silicon. b,c) Simulated TM mode optical profiles of the waveguide with GST on top in the amorphous and the crystalline state, respectively. Both were obtained using COMSOL MULTIPHYSICS. The dimensions of the waveguide were fixed to be 1.3 μm wide and 165 nm high. d) Optical microscopy image of an optical race-track resonator with GST switching section. e) Image of a micro Mach–Zehnder interferometer with a path difference of 200 μm between both arms. f) Balanced splitters used in the optical properties characterization of GST. All the beam splitters (BS) where built for 50:50 transmission.

balanced splitters (Figure 1f), light is coupled into the central grating coupler while two photoreceivers are used to record the transmitted signals at the outer ports. For accurate alignment of the fabricated samples with respect to the fiber array, we used a computer-controlled multiaxis piezostage with sub-100 nm positioning precision.

For each device configuration, we fabricated a large number of circuits with varying parameters in order to characterize the optical properties of the GST film. A colored SEM image of a 5 μm-wide GST strip on top of a nanophotonic waveguide is shown in **Figure 2**a. In Figure 2b, an atomic force microscopy (AFM) image of the PCM surface is depicted with an average root mean square (RMS) surface roughness of 2.4 nm for widths of 5, 10 and 20 μm, well below the wavelength of the guided optical mode. Residual spikes on both sides of the AFM image are due to the lack of directionality in the sputtering process, which results in GST deposition on the sidewalls.

For each device, transmission measurements were carried out at three different conditions: initially the nanocircuits were characterized before the GST deposition (after the first fabrication step) to obtain a reference transmission spectrum and also to calculate the intrinsic loss of each device. The second transmission measurement was done after the deposition of the GST strip. Thereby, we recorded the transmission spectra for

the devices in the amorphous state. A third measurement was done once the crystalline state of GST was reached. To transform GST from the amorphous into the crystalline state, the sample was heat-treated at 200 °C for 3 min on a hot-plate. The changes in structure before and after the thermal treatment can be observed in the X-ray diffraction (XRD) measurements shown in Figure 2c. The XRD data show a disordered distribution that turned into a characteristic fcc crystalline diffraction pattern when the GST was switched at a temperature around 150 °C. A further change occurs at around 300 °C, at which the GST transforms into the hexagonal phase.

To characterize the attenuation properties of the GST-$Si_3N_4$ waveguides, we analyzed the spectral properties of on-chip interferometers. Experimental results obtained from MZI devices with a waveguide width of 1.3 μm and grating couplers optimized for a central coupling wavelength $\lambda_c = 1595$ nm are shown in Figure 2d. Evenly spaced interference fringes in the amorphous (red) and the crystalline states (blue) with extinction ratio (ER) up to 40 dB are obtained, showing that the interferometer arms are closely balanced with low propagation loss. The measured interference pattern strongly depends on the state and the width $w$ of the GST. A red-shift of the fringe pattern is observed after switching which increases when $w$ becomes larger. The visibility of the fringes reduces gradually
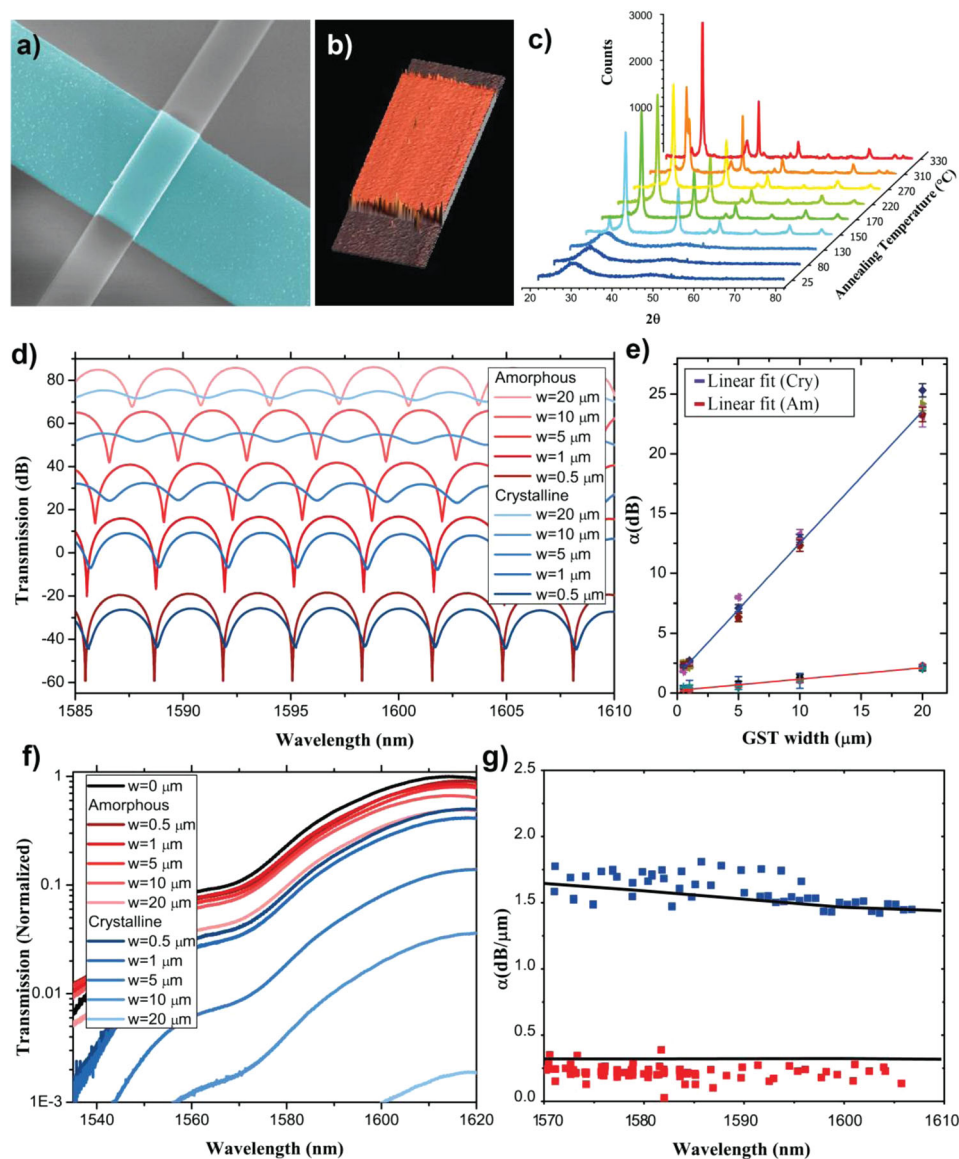
**Figure 2.** Optical characterization of GST-nanophotonic waveguides. a) Colored SEM image of a 5 μm wide GST strip on top of a waveguide. b) AFM image for the same GST strip in (a). The average RMS surface roughness was 2.4 nm. c) X-ray diffraction spectra for the GST at different annealing temperatures. d) Experimental interference patterns obtained from the MZI devices and measured for the amorphous and crystalline states for different GST widths $w$. The curves are offset vertically for clarity. The MZI devices had a waveguide width of 1.3 μm and central coupling wavelength $\lambda_c$ = 1595 nm. e) Attenuation coefficient $\alpha$ as a function of the GST width obtained from the interference patterns at the output of the MZI. Every point represents a single device and the lines represent the linear fit to the data in both states. f) Transmitted spectrum for different widths of GST in both states when using balance splitters. $w$ = 0 corresponds to the reference spectrum when no GST has been deposited. g) Comparison between the experimental results and FEM simulations for the attenuation coefficient per micron of GST. These results were obtained from rings resonators with 1 μm of GST on top.

with $w$ and so does the extinction ratio, defined as the ratio between the maximum ($P_{max}$) and the minimum ($P_{min}$) transmitted power. More important is the fact that, by measuring the ER, we were able to distinguish the state of the GST, and therefore switching can be detected. In addition, the calculation of the ER allowed us to calculate the attenuation coefficient $\alpha$ by means of Equation 1:[25]

$$ER = \frac{P_{out,max}}{P_{out,min}} = \left( \frac{1 + \exp(-\alpha \Delta l / 2)}{1 - \exp(-\alpha \Delta l / 2)} \right)^2 \tag{1}$$

where $P_{out}$ is the output power and $\Delta l$ is the path difference between the two arms of the MZI which was fixed at $\Delta l$ = 200 μm (see Figure 1e). In order to measure $\alpha$, four sets of MZI devices were prepared. The interferometers permute two different waveguide widths: 1.15 μm and 1.3 μm with two central wavelengths (defined by the grating coupler period) at $\lambda_c$ = 1595 nm and $\lambda_c$ = 1615 nm. Each kind of device was fabricated five times, one for each width of GST (500 nm, 1 μm, 5 μm, 10 μm, 20 μm). The extinction ratio was determined between $\lambda$ = 1590 nm and $\lambda$ = 1600 nm, and then the

Materials
Views
www.MaterialsViews.com

ADVANCED
MATERIALS
www.advmat.de

COMMUNICATION

attenuation coefficient was calculated according to Equation 1. We subtracted the attenuation coefficient of the devices without GST from the new values; this way we consider the attenuation exclusively due to the phase-change material. The results are depicted in Figure 2e. The linear fit to the experimental data yields the normalized attenuation coefficient, for the amorphous state $\alpha_{dB,AM}(w) = (0.095 \pm 0.005 \text{ dB } \mu m^{-1}) \, w + (0.21 \pm 0.05 \text{ dB})$ and $\alpha_{dB,CRY}(w) = (1.10 \pm 0.01 \text{ dB } \mu m^{-1}) \, w + (1.46 \pm 0.03 \text{ dB})$ for the crystalline state. The fitted value can be compared to numerical calculations using finite element simulations. From the imaginary part of the simulated modal effective refractive index $n_i$ the attenuation coefficient $\alpha$ can be calculated as $\alpha = 10 \log_{10} e \cdot 4\pi n_i / \lambda$ in units of dB per micrometer, which closely matches the measured result.

Additional experiments were carried out using the balanced splitters shown in Figure 1f for the same waveguide widths and $\lambda_c$ as in the MZIs. By measuring the transmission through both arms simultaneously, we were able to extract the attenuation coefficient by simply computing the ratio between the output power in the arm with GST on top and the output power in the reference arm (i.e., $w = 0$). In Figure 2f, the output power for both states and different GST width are depicted for the devices with a waveguide width of 1.3 µm and $\lambda_c = 1615$ nm. From the fit to the experimental data we obtained $\alpha_{dB,AM}(w) = (0.099 \pm 0.003 \text{ dB } \mu m^{-1}) \, w + (0.41 \pm 0.03 \text{ dB})$ and $\alpha_{dB,CRY}(w) = (1.08 \pm 0.01 \text{ dB } \mu m^{-1}) \, w + (1.25 \pm 0.08 \text{ dB})$ at $\lambda = 1595$ nm.

The attenuation coefficient for the GST can be obtained independently from the transmission spectra of race-track resonators by computing $\alpha_{dB} = 10 \log_{10} e \cdot 2\pi \frac{n_g}{\lambda Q}$,[26] where $Q$ is optical quality factor and $n_g$ is the group refractive index. The coefficient can be retrieved this way for all devices except for those with $w = 10$ and 20 µm in the crystalline state, because the resonance conditions are drastically damped by losses much higher than 6 dB. In this case the resonance peaks practically disappeared, making Lorentzian fitting challenging. With the data measured from the other devices and again subtracting the losses of the devices without GST, we obtained $\alpha_{dB,AM}(w) = (0.099 \pm 0.017 \text{ dB } \mu m^{-1}) \, w + (0.104 \pm 0.002 \text{ dB})$ and $\alpha_{dB,CRY}(w) = (1.14 \pm 0.05 \text{ dB } \mu m^{-1}) \, w + (0.16 \pm 0.08 \text{ dB})$ $\lambda = 1595$ nm. We used the results from the race-track resonators to compare $\alpha_{dB}$ as a function of the wavelength with simulation results obtained from finite element simulations. The results are plotted in Figure 2g, in which good agreement is observed without using any fit parameters when comparing with the guided transverse magnetic (TM) mode of the propagating light. Thus, the value for the attenuation per µm of GST (i.e., the slope of the linear fitting) is in good agreement for all three independent measurement approaches, taking into account a slight offset caused by different effects such as the losses in the waveguides, and imperfect coupling with the Bragg gratings. In the particular case of the MZI and balanced splitters, we note that the insertion loss introduced by the 50:50 beam splitters is also significant when comparing with the race-track resonators.

To demonstrate information storage and retrieval in the phase of GST using race-track resonators as memory elements, several sets of devices were fabricated for different waveguide widths, central wavelengths, coupling gaps between the resonator and the waveguide, and radius of curvature. Before the

GST deposition loaded optical $Q$-factors up to 70 000 were reached for the best devices. For resonators with a radius of 70 µm and a coupling gap of 1.3 µm, we found typical $Q$ factors on the order of 15 000; for larger rings with a radius of 100 µm and a coupling gap of 1.5 µm, the $Q$ factors increased to about 40 000. An optical microscopy image with an array of 25 memory elements with gaps between 0.5 and 1.5 µm, for five different GST widths and a curvature radius $r = 70$ µm is shown in **Figure 3**a. Depending on the resonance conditions of the race-tracks,[27,28] resonance peaks with different ER are observed in the power spectrum as shown in Figure 3b. A higher resolution spectrum shows one resonance peak in Figure 3c with a $Q$ factor of 18 780. The shown Lorentzian fit is used to extract the $Q$-factor by computing $Q = \lambda_{min}/\text{FWHM}$, where FWHM is the full width at half maximum and $\lambda_{min}$ corresponds to the wavelength at the minimum power, both obtained from the fitting curve. As stated above, the attenuation coefficient increases linearly with the width of the GST coverage and is higher for the crystalline state. Therefore, the $Q$-factor always decreases when switching the GST-covered section to the crystalline phase and by increasing the width of the section, as shown in **Table 1** for the race-track resonators with radius of 70 µm and coupling gap/waveguide width of 1.3 µm. Included in the Table are errors corresponding to the spread in $Q$ factor over the resonances within the wavelength window between 1590 and 1600 nm. This behavior can also be seen in Figure 3d where the FWHM of the resonance peaks for the same devices clearly increases when GST width is made wider. Moreover, in Table 1 the $Q$-factor dependence on the GST state is presented for a different and lower-loss set of race-track resonators with a radius of 100 µm and gap of 1.5 µm, using a waveguide width of 1.3 µm. Thus, by measuring the $Q$-factor, the phase state of GST can be read out and both states can be accurately differentiated.

When the attenuation inside the race-track changes, the resonance condition is altered as well,[28] which implies that optical resonators can be engineered in such a way that the ER increases or decreases when GST switches from the amorphous to the crystalline state. Here, the ER was directly computed by dividing the maximum value of each Lorentzian fit by the minimum. By doing so, we found a maximal change in ER for devices with a gap of 1.5 µm and radii of 40, 70 and 100 µm. In this configuration, the ER always decreased when switching from the amorphous to the crystalline state, allowing for accurate identification of the phase states. For devices with a gap of 1.3 µm and radii of 70 and 100 µm, the opposite situation occurs for GST widths of 0.5 µm and 1 µm. In these cases the $Q$ factor decreased from 14 930 ± 380 and 13 810 ± 290 to 11 320 ± 260 and 7440 ± 170, respectively, but the ER shows "inverse switching" (i.e., ER increases when going from the amorphous to the crystalline state), as depicted in Figure 3e, where the data were fitted to the analytical expression for ER with very good agreement. Therefore, optical switching either from low to high transmission or from high to low transmission is possible. The combination of both may be used to implement further logic operations when combining multiple memory elements. In addition, the wavelength shift of the minimum of the resonances can be used to detect switching between the states. The wavelength
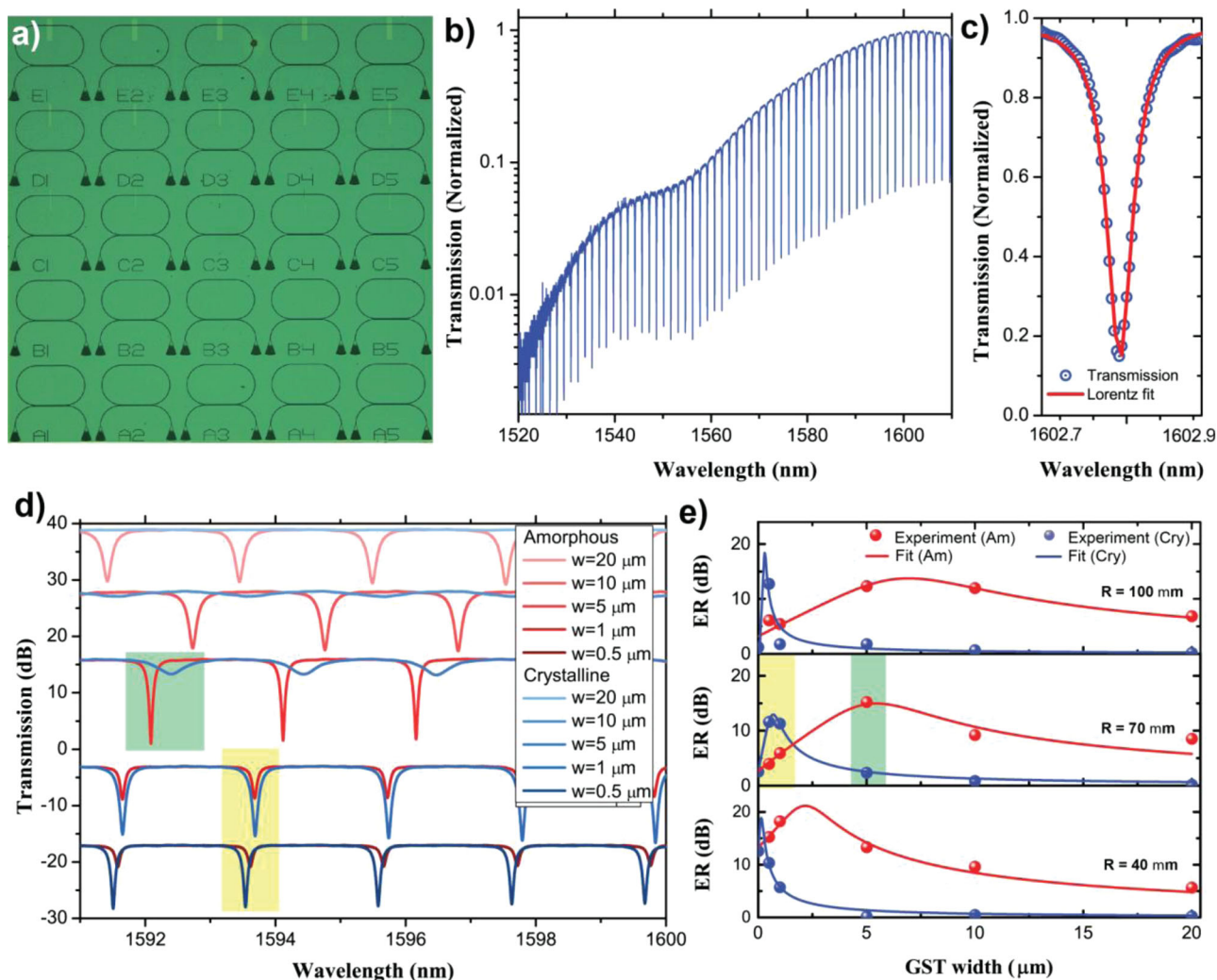
**Figure 3.** On-chip PCM memory elements. a) Optical microscopy image of an array with 25 different memory elements. In the horizontal direction the gap between waveguide and resonator was varied from 0.5, 0.7, 1.0, 1.3 to 1.5 μm. In the vertical direction, five GST widths from 0.5 μm (bottom) to 20 μm (top) were used. b) Typical transmission spectrum measured for race-track resonators. c) Higher resolution spectrum of one of the resonance peaks shown in (b) with a *Q*-factor of 18 780. Also shown is the Lorentzian fit to the experimental data. d) Comparison between resonances in the crystalline and amorphous states for different GST widths. Switching and "inversed switching" are observed in the highlighted regions in green and yellow, respectively. The relative shift of the central wavelength can be observed as well as the reduction of the *Q*-factor when peaks get broader. e) ER obtained for different race-track radius (*R*) as a function of GST width and state. The highlighted regions correspond to those highlighted in (d) and the lines correspond to the fits obtained using the analytical function for ER.

shift is especially pronounced for widths larger than 5 μm reaching about 0.4 nm. By measuring the position of the resonance peak, the state of the GST can thus be retrieved. As recently shown for silicon based optical resonators,[29] such devices will therefore also be suitable for implementing optically tunable devices on chip.

**Table 1.** Average *Q*-factors for peak resonances in the range 1590–1600 nm as a function of the GST width and phase state.

|  |  | *w* = 0.5 μm | *w* = 1 μm | *w* = 5 μm | *w* = 10 μm | *w* = 20 μm |
|---|---|---|---|---|---|---|
| *R* = 70 μm Gap = 1.3 μm | Without GST | 16 190 ± 470 | 15 740 ± 250 | 14 050 ± 280 | 11 075 ± 75 | 13 780 ± 280 |
|  | Amorphous | 14 930 ± 380 | 13 810 ± 290 | 10 430 ± 200 | 6010 ± 100 | 5860 ± 40 |
|  | Crystalline | 11 320 ± 260 | 7440 ± 170 | 2840 ± 280 | 2600 ± 1500 | — |
| *R* = 100 μm Gap = 1.5 μm | Without GST | 29 410 ± 420 | 42 740 ± 610 | 37 800 ± 620 | 26 450 ± 330 | 45 450 ± 660 |
|  | Amorphous | 26 130 ± 320 | 32 060 ± 600 | 21 020 ± 200 | 14 290 ± 130 | 10 150 ± 50 |
|  | Crystalline | 18 150 ± 490 | 12 480 ±150 | 5080 ± 50 | — | — |

In conclusion, we have presented a tunable hybrid platform combining nanophotonic circuits with phase-change materials. Using nanoscale chalcogenide sections, the transmission properties of optical circuits can be strongly altered by inducing phase-transitions in the PCM. We found good agreement amongst the results from three different nanophotonic architectures, and showed experimentally that optical switching can be detected when GST is transformed from the amorphous to the crystalline state. Using race-track resonators as memory elements, optical parameters such as the $Q$-factor, the central wavelength of the peak resonances, and the ER can be used to retrieve the state of the GST accurately. Our results are the first step towards optically tunable photonic circuits that can potentially be switched on a picosecond timescale as we proposed previously.[16] Nanoscale hybrid sections are sufficient to route optical signals on chip, and therefore the approach holds promise for low-power operation and photonic memories on a chip. Because the phase state is retained after switching, the devices are inherently non-volatile, a key-step towards non-von Neumann arithmetic processing.[30–32] Our results indicate not only that non-volatile all-optical memories will be available in the near future, but also that it may even be possible to perform arithmetic operations entirely in the photonic domain on a single chip.

## Experimental Section

*Sample Fabrication*: The fabrication process was divided into two main steps. In the first step, photonic circuitry is realized using electron-beam lithography in Ma-N 2403 negative tone resist on a JEOL JBX-5500ZD 50 kV system. After developing the sample, a reflow process of 90 s at 100 °C was applied to reduce the intrinsic roughness of the resist and thus to improve the transmission of the devices.[23] Reactive ion etching in $CHF_3/O_2$ was carried out to etch 165 nm of $Si_3N_4$ at a rate of 1.04 nm s$^{-1}$. Subsequently, the devices were measured to obtain the reference transmission before GST deposition.

The second step involved a lift-off process to pattern GST. This was achieved by a second electron-beam lithography exposure. 240 nm of a poly(methyl methacrylate) (PMMA) positive tone resist were spin-coated on top of the sample. Thereafter, rectangular patterns of 0.5, 1, 5, 10, and 20 μm wide and 80 μm long were patterned, such that their widths ran parallel to the sides of the waveguides (Figure 1d–f). After developing the PMMA, 10 nm of GST were sputtered onto the sample followed by deposition of 10 nm of ITO (to avoid oxidation of the PCM). Finally, lift-off of the GST/ITO stack was carried to complete the nanophotonic-chalcogenide circuits.

## Acknowledgements

[1] E. R. Meinders, A. V. Mijritskii, L. van Pieterson, M. Wuttig, *Optical Data Storage: Phase Change Media and Recording*, Springer, Berlin, Germany **2006**.

[2] M. Wuttig, N. Yamada, *Nat. Mater.* **2007**, *6*, 824.

[3] D. Lencer, M. Salinga, M. Wuttig, *Adv. Mater.* **2011**, *23*, 2030.

[4] S.-H. Lee, Y. Jung, R. Agarwal, *Nat. Nanotechnol.* **2007**, *2*, 626.

[5] N. Yamada, T. Matsunaga, *J. Appl. Phys.* **2000**, *88*, 7020.

[6] S. Raoux, G. W. Burr, M. J. Breitwisch, C. T. Rettner, Y. C. Chen, R. M. Shelby, M. Salinga, D. Krebs, S. H. Chen, H. L. Lung, C. H. Lam, *IBM J. Res. Dev.* **2008**, *52*, 465.

[7] S. Kim, B. J. Bae, Y. Zhang, R. G. D. Jeyasingh, Y. Kim, I. G. Baek, S. Park, S. W. Nam, H.-S. P. Wong, *IEEE Trans. Electron Devices* **2011**, *58*, 1483.

[8] S. R. Ovshinsky, *Phys. Rev. Lett.* **1968**, *21*, 1450.

[9] B.-S. Lee, J. R. Abelson, S. G. Bishop, D.-H. Kang, B.-K Cheong, K.-B Kim, *J. Appl. Phys.* **2005**, *97*, 093509.

[10] J. Siegel, A. Schropp, J. Solis, C. N. Alfonso, M. Wuttig, *Appl. Phys. Lett.* **2004**, *84*, 2250.

[11] G. Bruns, P. Merkelbach, C. Schlockermann, M. Salinga, M. Wuttig, T. D. Happ, J. B. Phillip, M. Kund, *Appl. Phys. Lett.* **2009**, *95*, 043108.

[12] A. V. Kolobov, P. Fons, A. I. Frenkel, A. L. Ankudinov, J. Tominaga, T. Uruga, *Nat. Mater.* **2004**, *3*, 703.

[13] B. Jalali, S. Fathpour, *J. Lightwave Technol.* **2006**, *24*, 4600.

[14] Q. F. Xu, B. Schmidt, S. Pradhan, M. Lipson, *Nature* **2007**, *435*, 325.

[15] G. T. Reed, G. Mashanovich, F. Y. Gardes, D. J. Thomson, *Nat. Photonics* **2010**, *4*, 518.

[16] W. H. P. Pernice, H. Bhaskaran, *App. Phys. Lett.* **2012**, *101*, 171101.

[17] M. Bagheri, M. Poot, M. Li, W. Pernice, H. X. Tang, *Nat. Nanotechnol.* **2011**, *6*, 726.

[18] F. Marquardt, S. M. Girvin, *Physics* **2009**, *2*, 40.

[19] T. J. Kippenberg, K. J. Vahala, *Science* **2008**, *321*, 1172.

[20] W. K. Njoroge, H. W. Woltgens, M. Wuttig, *J. Vac. Sci. Technol. A* **2002**, *20*, 230.

[21] S. Y. Kim, S. J. Kim, H. Seo, M. R. Kim, *Proc. SPIE* **1998**, *3401*, 112.

[22] K. Fong, W. Pernice, M. Li, H. Tang, *Appl. Phys. Lett.* **2010**, *97*, 073112.

[23] A. Gondarenko, J. A. Levy, M. Lipson, *Opt. Express* **2009**, *17*, 11366.

[24] H. Kim, C. M. Gilmore, A. Piqué, J. S. Horwitz, H. Mattoussi, H. Murata, Z. H. Kafafi, D. B. Chrisey, *J. Appl. Phys.* **1999**, *86*, 6451.

[25] H. Li, Y. Anugrah, S. J. Koester, M. Li, *Appl. Phys. Lett.* **2012**, *101*, 111110.

[26] P. Rabiei, W. H. Steier, C. Zhang, L. R. Dalton, *J. Lightwave Technol.* **2002**, *20*, 1968.

[27] G. T. Reed, W. R. Headley, F. Y. Gardes, B. D. Timotijevic, S. P. Chan, G. Z. Mashanovich, *Proc. SPIE* **2006**, *6183*, 61830G.

[28] W. Bogaerts, P. De Heyn, T. Van Vaerenbergh, K. De Vos, S. K. Selvaraja, T. Claes, P. Dumon, P. Bienstman, D. Van Thourhout, R. Baets, *Laser Photonics Rev* **2012**, *6*, 47.

[29] M. Rude, J. Pello, R. E. Simpson, J. Osmond, G. Roelkens, J. J. G. M. van der Tol, V. Pruneri, *Appl. Phys. Lett.* **2013**, *103*, 141119

[30] C. D. Wright, P. Hosseini, J. A. Vazquez-Diosdado, *Adv. Funct. Mater.* **2013**, *23*, 2248.

[31] C. D. Wright, Y. Liu, K. I. Kohary, M. M. Aziz, R. J. Hicken, *Adv. Mater.* **2011**, *23*, 3408.

[32] S. R. Ovshinsky, *Jpn. J. Appl. Phys. Lett.* **2004**, *43*, 4695.